

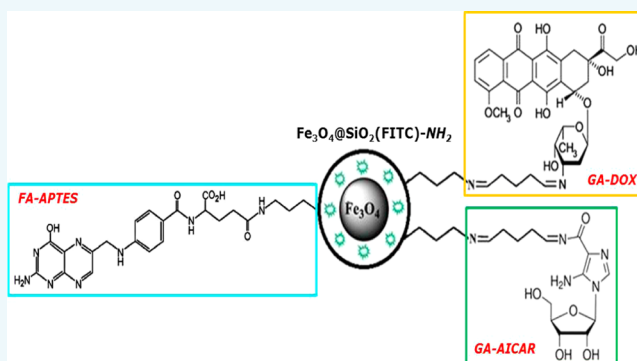
Synthesis and Characterization of AICAR and DOX Conjugated Multifunctional Nanoparticles as a Platform for Synergistic Inhibition of Cancer Cell Growth

Cenk Daglioglu^{*,†,‡} and Burcu Okutucu[†]

[†]Ege University, Faculty of Science, Biochemistry Department, Bornova/Izmir 35040, Turkey

[‡]Izmir Institute of Technology, Faculty of Science, Department of Molecular Biology and Genetics, Urla/Izmir 35430, Turkey

ABSTRACT: The success of cancer treatment depends on the response to chemotherapeutic agents. However, malignancies often acquire resistance to drugs if they are used frequently. Combination therapy involving both a chemotherapeutic agent and molecularly targeted therapy may have the ability to retain and enhance therapeutic efficacy. Here, we addressed this issue by examining the efficacy of a novel therapeutic strategy that combines AICAR and DOX within a multifunctional platform. In this context, we reported the bottom-up synthesis of $\text{Fe}_3\text{O}_4@(\text{FITC})\text{-FA/AICAR/DOX}$ multifunctional nanoparticles aiming to neutralize survivin (BIRC5) to potentiate the efficacy of DOX against chemoresistance. The structure of nanoparticles was characterized by dynamic light scattering (DLS), zeta-potential measurement, X-ray diffraction (XRD), Fourier transform infrared spectroscopy (FT-IR), thermogravimetric analysis (TGA), and electron microscopy (SEM and STEM with EDX) techniques. Cellular uptake and cytotoxicity experiments demonstrated preferentially targeted delivery of nanoparticles and an efficient reduction of cancer cell viability in five different tumor-derived cell lines (A549, HCT-116, HeLa, Jurkat, and MIA PaCa-2). These results indicate that the multifunctional nanoparticle system possesses high inhibitory drug association and sustained cytotoxic effect with good biocompatibility. This novel approach which combines AICAR and DOX within a single platform might be promising as an antitumor treatment for cancer.



INTRODUCTION

Chemotherapy is one of the principal modes of treatment for cancer, but the effectiveness of chemotherapy is limited by drug resistance.¹ Chemotherapeutic agents are generally used in combination with a maximum tolerated dose to eliminate drug resistance and then to achieve maximum cancer cell killing.² However, most patients do not respond to these drugs and they often experience severe adverse effects because of greater toxicity compared to each drug alone.³ One of the major factors responsible for chemoresistance is the evolution of the tumor cells toward a phenotype that is resistant to apoptotic cell kill. On a molecular level, increased expression of the inhibitor of apoptosis protein family (IAPs) has been detected in this phenotype.⁴ Therefore, interfering with IAPs expression or function is a new strategy to eliminate drug resistance. Survivin, a structurally unique member of the IAP family that acts as a suppressor of apoptosis and plays a central role in cell division, is overexpressed in all human cancers, but demonstrates low expression in normal tissues.⁵ Several preclinical studies in different human tumor models have demonstrated that downregulation of survivin expression or function, accomplished by means of various strategies, reduced tumor growth potential, increased the apoptotic rate, and sensitized tumor cells to chemotherapeutic drugs.⁶ Heat shock

protein 90 (Hsp90) is a significant target in the development of rational cancer therapy due to its role at the crossroads of multiple signaling pathways associated with cell proliferation and cell viability. Through combined structure- and dynamics-based computational design strategy and experimental tests, Meli et al. reported that the nonpeptidic small molecule 5-aminoimidazole-4-carboxamide-1- β -D-ribofuranoside (AICAR) binds the Hsp90 N-domain, destabilizes multiple Hsp90 client proteins in vivo, including survivin, and exhibits antiproliferative and proapoptotic activity in multiple tumor cell lines, while not affecting proliferation of normal human fibroblasts.⁷ Doxorubicin (DOX) is a common chemotherapeutic used in the treatment of a wide range of cancers because of its excellent antitumor activity.⁸ Resistance to this agent impairs treatment of cancer patients and prevents successful treatment.⁹ In addition, DOX has a relatively low therapeutic index and its clinical usage is limited due to acute and chronic toxicities such as immunosuppression and cardiotoxicity.¹⁰ Therefore, more efficient treatment strategies must be developed that reduce or eliminate drug resistance,

Received: February 11, 2016

Revised: March 17, 2016

Published: March 20, 2016

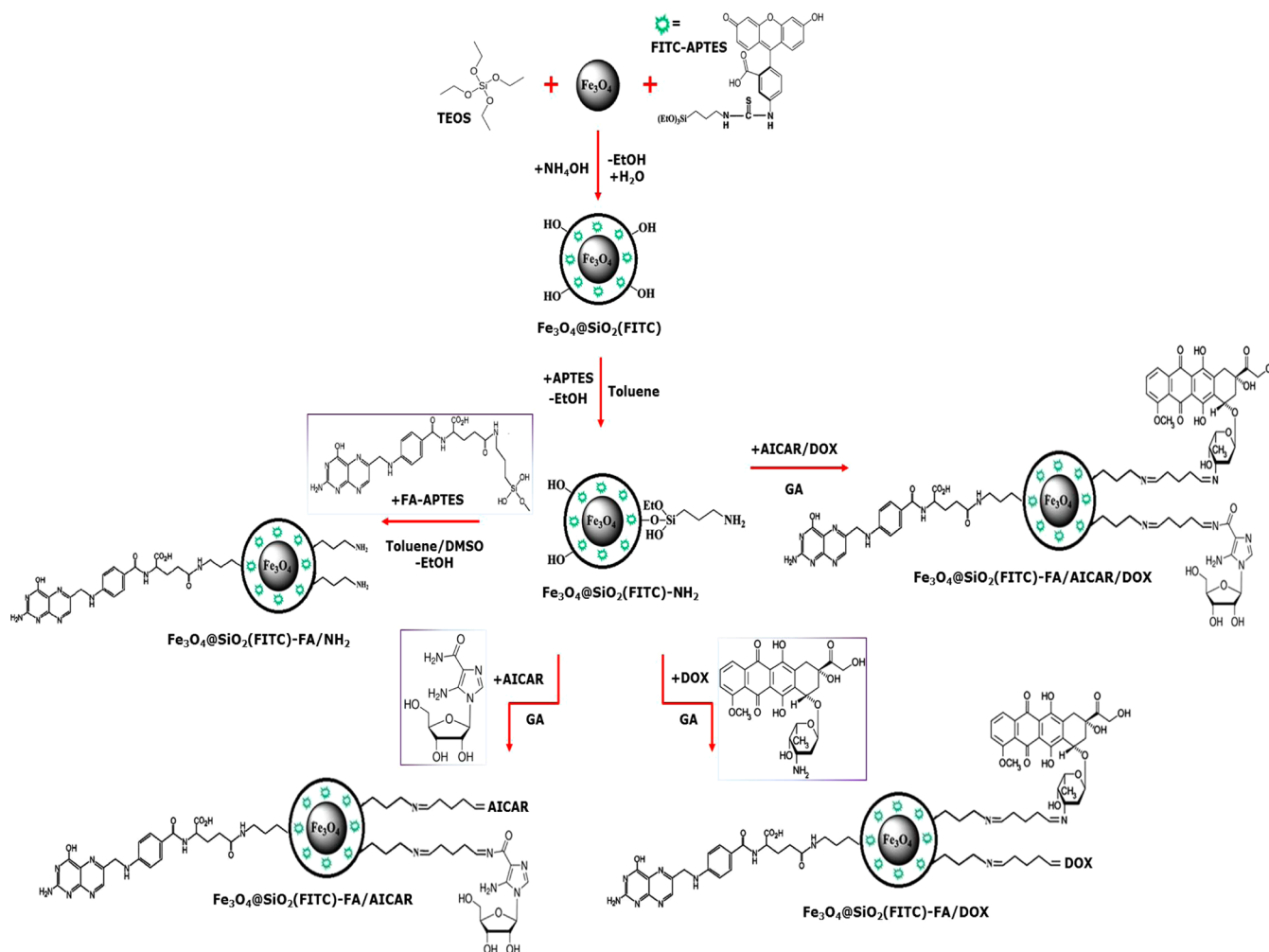


Figure 1. Reaction schemes to generate (1) Fe₃O₄@SiO₂(FITC); (2) Fe₃O₄@SiO₂(FITC)-FA/NH₂; (3) Fe₃O₄@SiO₂(FITC)-FA/AICAR; (4) Fe₃O₄@SiO₂(FITC)-FA/DOX; and (5) Fe₃O₄@SiO₂(FITC)-FA/AICAR/DOX nanoparticles.

decrease the cytotoxic effects of DOX, and also enhance therapeutic efficacy. Considering the potential value of reducing or abolishing survivin expression as a means of overcoming chemoresistance, we have successfully developed a core/shell type of nanoparticle formulation to codeliver AICAR and DOX, thereby enhancing antitumor activity while reducing chemoresistance.

In recent years, multifunctional particles with magnetism, fluorescence, and target navigation have been explored extensively in biomedical applications. They have been developed as an all-in-one biomedical platform for simultaneous fluorescence imaging, manipulation of cells, and drug delivery tools.^{11–14} Among the various multifunctional particles, dye-doped silica magnetic-fluorescent composites are very promising biomedical materials due to the following advantages: (1) their high photostability and relatively strong fluorescent signal owing to their high dye-incorporation capabilities and stabilization in a protective silica matrix with biocompatibility and less toxicity; (2) superparamagnetic oxide iron nanoparticles with fast magnetic response making it easy to manipulate via an external magnetic field, and this “remote control” providing considerable advantages for many applications;¹⁵ (3) contrast agents with both optical and magnetic contrast serving as good molecular imaging probes both *in vitro* and *in vivo*.¹⁶ In addition, active targeting of nanoparticles can potentially increase the

efficacy and reduce the toxicity of therapeutic agents.¹⁷ This is achieved by conjugating the surface of nanoparticles using specific cell ligands. Folic acid (FA) has been widely used in the delivery of anticancer agents due to its small size, low cost, high tumor tissue specificity, nonimmunogenic nature, and fast internalization through the cellular membrane.¹⁸ FA linked nanocarriers have fairly high binding affinity to folate receptors (FR) expressed on tumor cells.¹⁹

In this study we have rationally designed the bottom-up synthesis of four successive nanoparticles: (1) Fe₃O₄@SiO₂(FITC)-FA nanoparticles noncontaining any inhibitor or drug; (2) Fe₃O₄@SiO₂(FITC)-FA/AICAR nanoparticles containing only inhibitor; (3) Fe₃O₄@SiO₂(FITC)-FA/DOX nanoparticles containing only drug; (4) Fe₃O₄@SiO₂(FITC)-FA/AICAR/DOX nanoparticles containing both inhibitor and drug to evaluate synergistic potential of therapeutics. The feasibility of nanoparticles was evaluated by investigating their capability in cellular uptake, fluorescent imaging, and cytotoxic effect in five different tumor-derived cell lines (A549, HCT-116, HeLa, Jurkat, and MIA PaCa-2). To the best of our knowledge, this is the first study which combines AICAR and DOX as therapeutic agents and examines their synergistic effect within a multifunctional platform. The preliminary cell tests confirm the potential of these multifunctional nanoparticles as an antitumor treatment in cancer therapy.

Table 1. Immobilization Yields of AICAR and DOX on Silica Surface

| immobilization method | GA concentration (%) | AICAR and DOX immobilization yield (%) | AICAR and DOX immobilization concentration (μM per mg nanoparticles) |
|--|----------------------|--|--|
| $\text{Fe}_3\text{O}_4@SiO_2(\text{FITC})\text{-FA/AICAR}$ | 0.1 | 6.8 | 1.3 |
| | 1.0 | 30.5 | 6.1 |
| $\text{Fe}_3\text{O}_4@SiO_2(\text{FITC})\text{-FA/DOX}$ | 0.1 | 10.1 | 0.2 |
| | 1.0 | 51.5 | 1.0 |
| $\text{Fe}_3\text{O}_4@SiO_2(\text{FITC})\text{-FA/AICAR/DOX}$ | 0.1 | 11.2 _{(AICAR) / 10.5_(DOX)} | 2.2 _{(AICAR) / 0.2_(DOX)} |
| | 1.0 | 22.5 _{(AICAR) / 35.7_(DOX)} | 4.5 _{(AICAR) / 0.7_(DOX)} |

RESULTS AND DISCUSSION

Synthesis and Characterization of Multifunctional Nanoparticles. To construct the nanoparticles, silica (SiO_2) was used for surface coating of Fe_3O_4 particles because dye molecules can be easily incorporated into a silica shell, and silica is quite biocompatible and resistant to biodegradation in biological environments.²⁴ In addition, silica can be easily surface functionalized for bioconjugation and targeted for various applications in biological systems. Hence, in this study we first synthesized bifunctional nanoparticles, $\text{Fe}_3\text{O}_4@SiO_2(\text{FITC})$ (Figure 1) with both fluorescent and magnetic properties by sol–gel formation of the silica layer onto the magnetite surface. To increase the cellular uptake of magnetic iron oxide particles, nanoparticles were vectorized with folic acid by silanization FA-APTES conjugate on the silica surface and simultaneously the surfaces were modified with free APTES to form an amine-terminated overlayer for the subsequent conjugation of both AICAR and DOX via Schiff-base formation. In general, two different approaches have been explored for drug transportation by nanoparticles. The first consists of conjugating the drugs covalently to the nanoparticle surface through appropriate linkers, and the second in physically adsorbing or establishing ionic and hydrogen bonds. The covalent method is the most used because the bond strength makes nanoparticle–drug conjugates highly stable.²⁵ Thus, after surface modification with APTES, AICAR and DOX were covalently linked on the surface of nanoparticles from their amine group using glutaraldehyde as a linker. In this step, different concentrations of glutaraldehyde were tested separately to determine the optimal linker concentration (Table 1). Among the tested amounts of glutaraldehyde, the highest coupling yield of AICAR and DOX complexes was observed at 1% glutaraldehyde concentration. The amount of bound AICAR or DOX was calculated from the difference between the amount of AICAR or DOX introduced into the coupling reaction mixture and the amount of AICAR or DOX present in the washing water after immobilization by measuring AICAR or DOX absorbance at 260 and 480 nm, respectively.

The average hydrodynamic diameter of the oleic acid stabilized Fe_3O_4 nanoparticles, determined for 0.1/0.2/0.4/0.6 mL concentrations of oleic acid by DLS, were 4.9 ± 1.2 , 7.8 ± 1.5 , 12.1 ± 3.8 , and 18.7 ± 7 nm, respectively. Since oleic acid effectively regulates Fe_3O_4 nanoparticle growth and prevents aggregation, different amounts of oleic acid were tested to produce size-controlled monodisperse Fe_3O_4 nanoparticles. The nanoparticle sizes increased regularly with increasing amount of oleic acid, due to increased chemisorption of oleate ions on the magnetite particles. Therefore, we chose the nanoparticles stabilized with 0.1 mL oleic acid in the next study to obtain the proper nanoparticles with narrow size distribution. The silica coating led to an increase of the average particle size (~ 17 nm) (Table 2). After the immobilization

Table 2. Size and Zeta Potential of the Multifunctional Nanoparticles

| nanoparticles | size (nm) | zeta potential (mV) |
|--|----------------|---------------------|
| $\text{Fe}_3\text{O}_4@SiO_2(\text{FITC})$ | 17.2 ± 3.5 | -17.5 ± 1.1 |
| $\text{Fe}_3\text{O}_4@SiO_2(\text{FITC})\text{-FA/NH}_2$ | 29.7 ± 6.2 | $+5.3 \pm 2.3$ |
| $\text{Fe}_3\text{O}_4@SiO_2(\text{FITC})\text{-FA/AICAR}$ | 53.5 ± 6.7 | -9.1 ± 1.6 |
| $\text{Fe}_3\text{O}_4@SiO_2(\text{FITC})\text{-FA/DOX}$ | 62.5 ± 8.6 | -8.4 ± 1.5 |
| $\text{Fe}_3\text{O}_4@SiO_2(\text{FITC})\text{-FA/AICAR/DOX}$ | 79.2 ± 8.2 | -11.3 ± 3.4 |

process, the size of nanoparticles attached with both AICAR and DOX increased to approximately 79 nm. Particles with a diameter ranging from 10 to 100 nm are optimal for intravenous injection and have the most prolonged blood circulation times. These particles are small enough to evade the Reticuloendothelial System (RES) of the body as well as to penetrate small capillaries of the tissues and offer the most effective distribution in targeted tissues.²⁶

The zeta potential of nanoparticles was analyzed to confirm the change in their surface potential due to proper biofunctionalization. The stepwise conjugation of functional groups on the silica surface was monitored by measuring the surface charges at different stages of synthesis (Figure 2 and Table 2). A negative zeta potential (ζ) value of -17.5 mV (pH 7.4) of $\text{Fe}_3\text{O}_4@SiO_2(\text{FITC})$ nanoparticles can be attributed to the presence of ionizable silanol groups of silica surface. After modification with APTES/FA conjugate, the zeta potential value of $\text{Fe}_3\text{O}_4@SiO_2(\text{FITC})\text{-FA/NH}_2$ nanoparticles reverted to a positive value ($+5.3$ mV at pH = 7.4) due to the presence of an excess of positively charged amino groups. FA is expected to furnish silica surface with negative charge; however, the excess amount of NH_2 groups presumably nullify the FA charge and make the overall surface charge slightly positive. Further modification of the surface by conjugating both AICAR or DOX groups reverted the surface charge back to a negative value, for $\text{Fe}_3\text{O}_4@SiO_2(\text{FITC})\text{-FA/AICAR}$, $\text{Fe}_3\text{O}_4@SiO_2(\text{FITC})\text{-FA/DOX}$, and $\text{Fe}_3\text{O}_4@SiO_2(\text{FITC})\text{-FA/AICAR/DOX}$ nanoparticles with average values of -9.1 , -8.4 , and -11.3 mV obtained at pH = 7.4, respectively. These results could be attributed to a function of the ionizability of AICAR and DOX groups on silica surface.

The bulk crystal structure of the nanoparticles was analyzed by X-ray diffraction (XRD) using the Debye–Scherrer method. Figure 3 shows the XRD patterns of the Fe_3O_4 and $\text{Fe}_3\text{O}_4@SiO_2(\text{FITC})$ nanoparticles. For Fe_3O_4 magnetic particles, XRD spectra showed the six characteristic peaks occurring at 2θ of 30.1, 35.5, 43.1, 53.4, 57.0, and 62.6, which are marked by their corresponding indices (220), (311), (400), (422), (511), and (440), respectively. These results were in excellent agreement with the JCPDS file for Fe_3O_4 (Card No. #19–629). This analysis revealed that the prepared magnetic particles are pure Fe_3O_4 with a cubic spinel structure. For $\text{Fe}_3\text{O}_4@SiO_2(\text{FITC})$ nanoparticles, the same six characteristic peaks corresponding

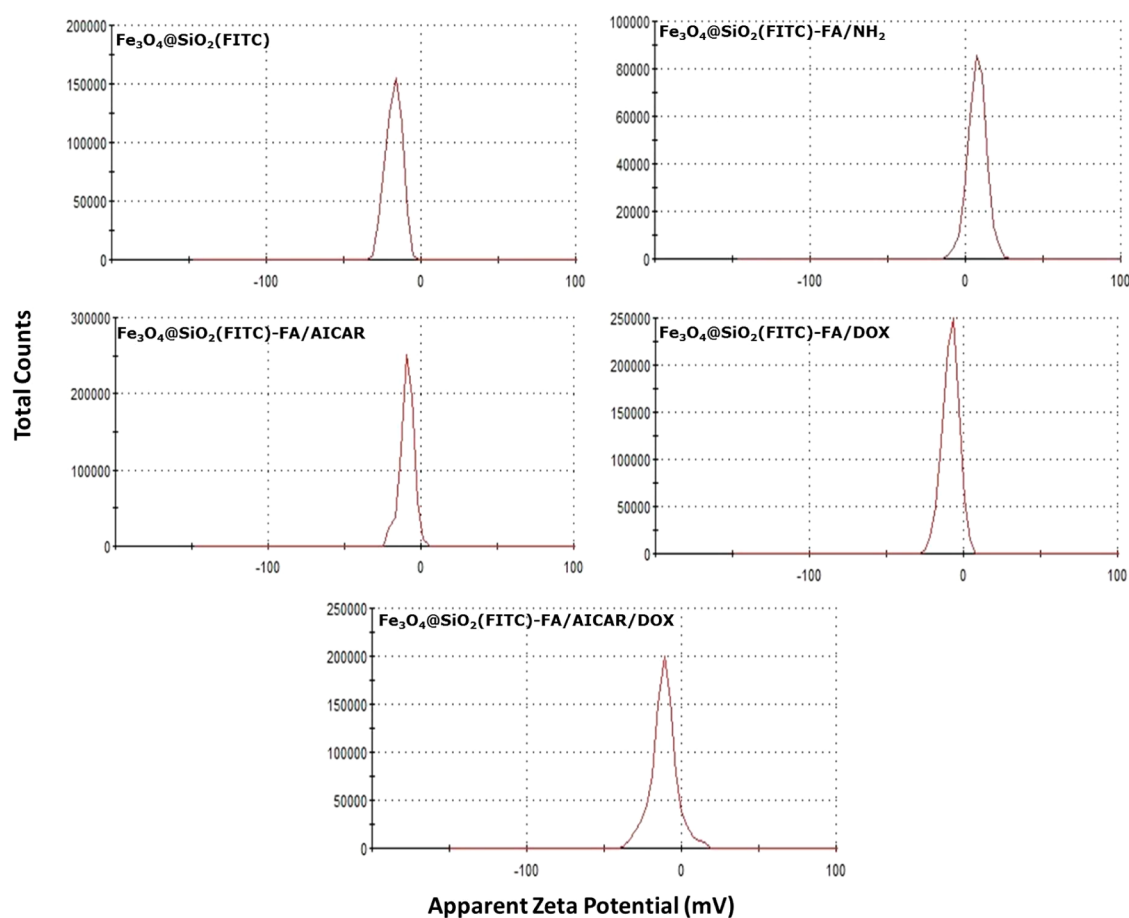


Figure 2. Zeta potential measurements of (1) $\text{Fe}_3\text{O}_4@SiO_2(\text{FITC})$; (2) $\text{Fe}_3\text{O}_4@SiO_2(\text{FITC})\text{-FA/NH}_2$; (3) $\text{Fe}_3\text{O}_4@SiO_2(\text{FITC})\text{-FA/AICAR}$; (4) $\text{Fe}_3\text{O}_4@SiO_2(\text{FITC})\text{-FA/DOX}$; and (5) $\text{Fe}_3\text{O}_4@SiO_2(\text{FITC})\text{-FA/AICAR/DOX}$ nanoparticles obtained at pH = 7.4 using DLS.

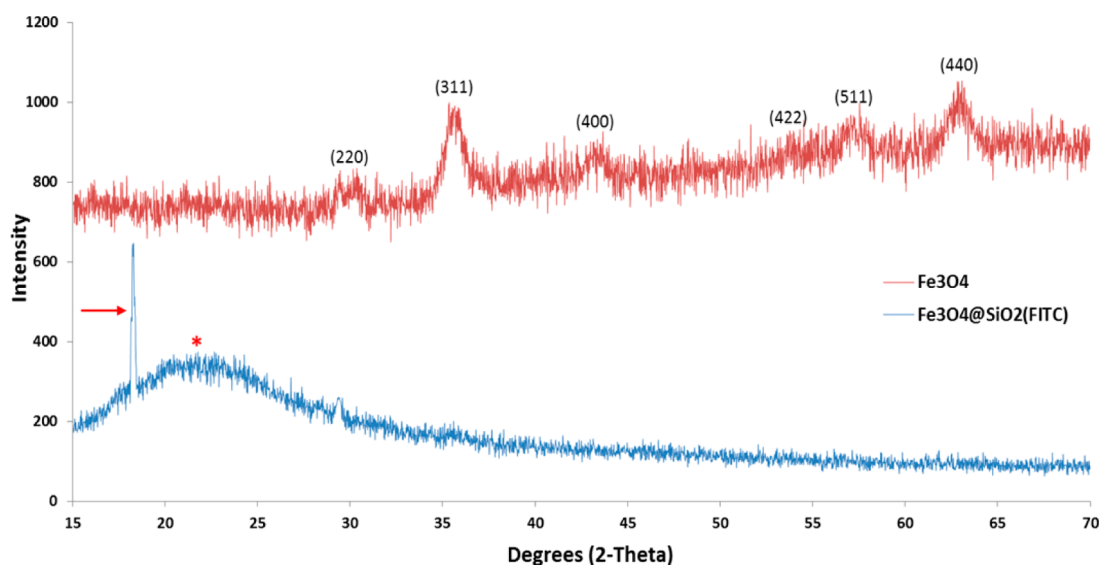


Figure 3. Powder XRD patterns of Fe_3O_4 and $\text{Fe}_3\text{O}_4@SiO_2(\text{FITC})$ nanoparticles. The position of the peak of FITC and the broad peak of amorphous silica are marked with a red arrow and asterisk (*), respectively.

to uncoated Fe_3O_4 were significantly masked and a broad peak ranging from 15° to 30° confirmed the presence of an amorphous silica shell surrounding the Fe_3O_4 magnetic core.²⁷ This result indicated that the silica coating did not cause a phase change in the magnetic particles. Therefore, the magnetic particles could preserve their magnetic properties for further

applications. Simultaneously, the characteristic peak at 2θ of 18.1° was observed for the fluorescent FITC, which exists in the silica layer in samples.²⁸

The surface modification and conjugation of nanoparticles with APTES, FA, AICAR, and DOX were confirmed by Fourier transform infrared (FTIR) spectroscopy. For comparison,

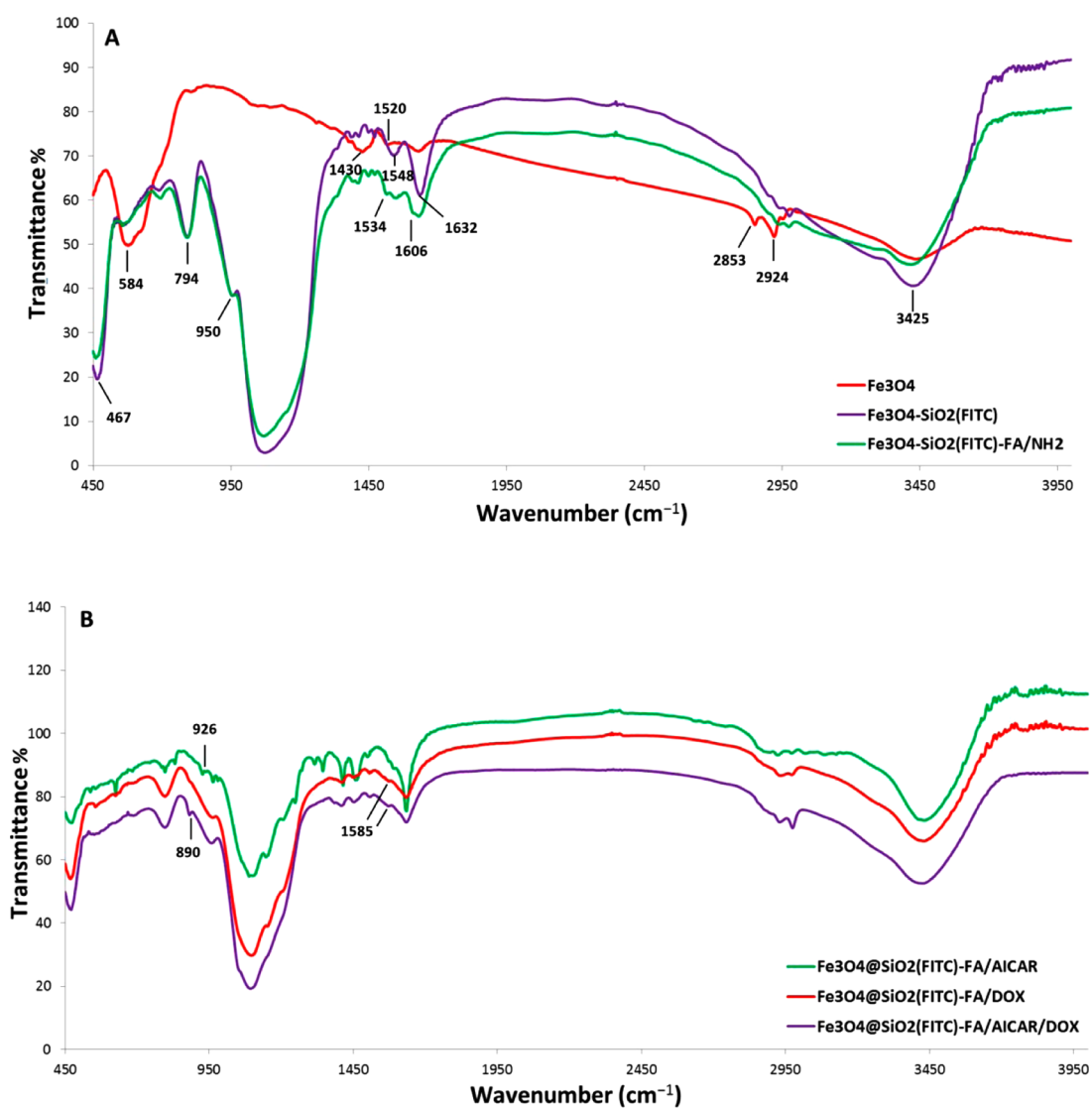


Figure 4. FTIR characterization of (A) Fe₃O₄, Fe₃O₄@SiO₂(FITC), Fe₃O₄@SiO₂(FITC)-FA/NH₂; (B) Fe₃O₄@SiO₂(FITC)-FA/AICAR, Fe₃O₄@SiO₂(FITC)-FA/DOX, and Fe₃O₄@SiO₂(FITC)-FA/AICAR/DOX nanoparticles.

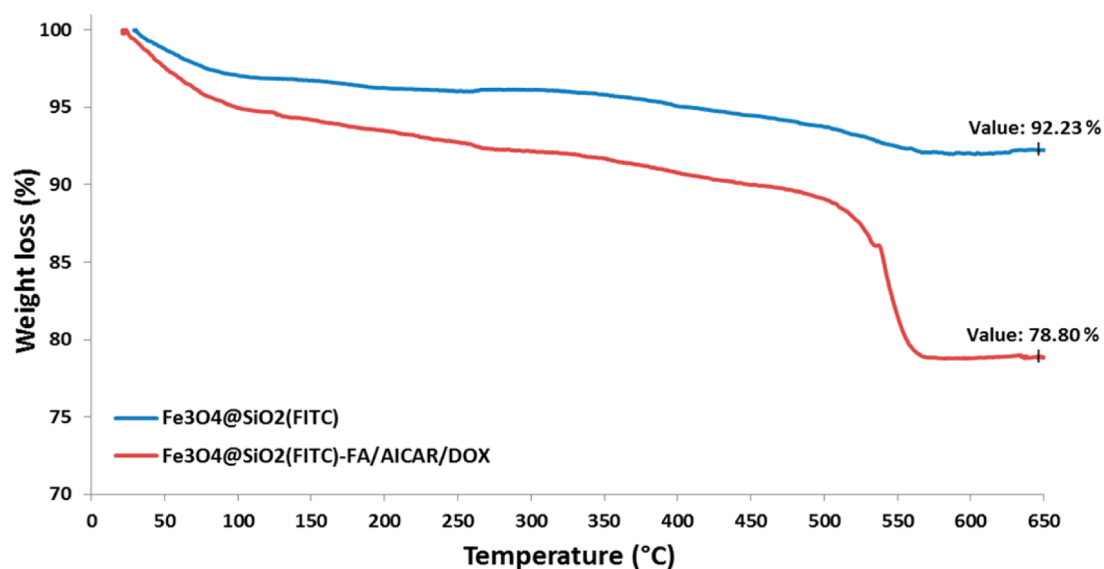


Figure 5. TGA trace of Fe₃O₄@SiO₂(FITC) and Fe₃O₄@SiO₂(FITC)-FA/AICAR/DOX nanoparticles.

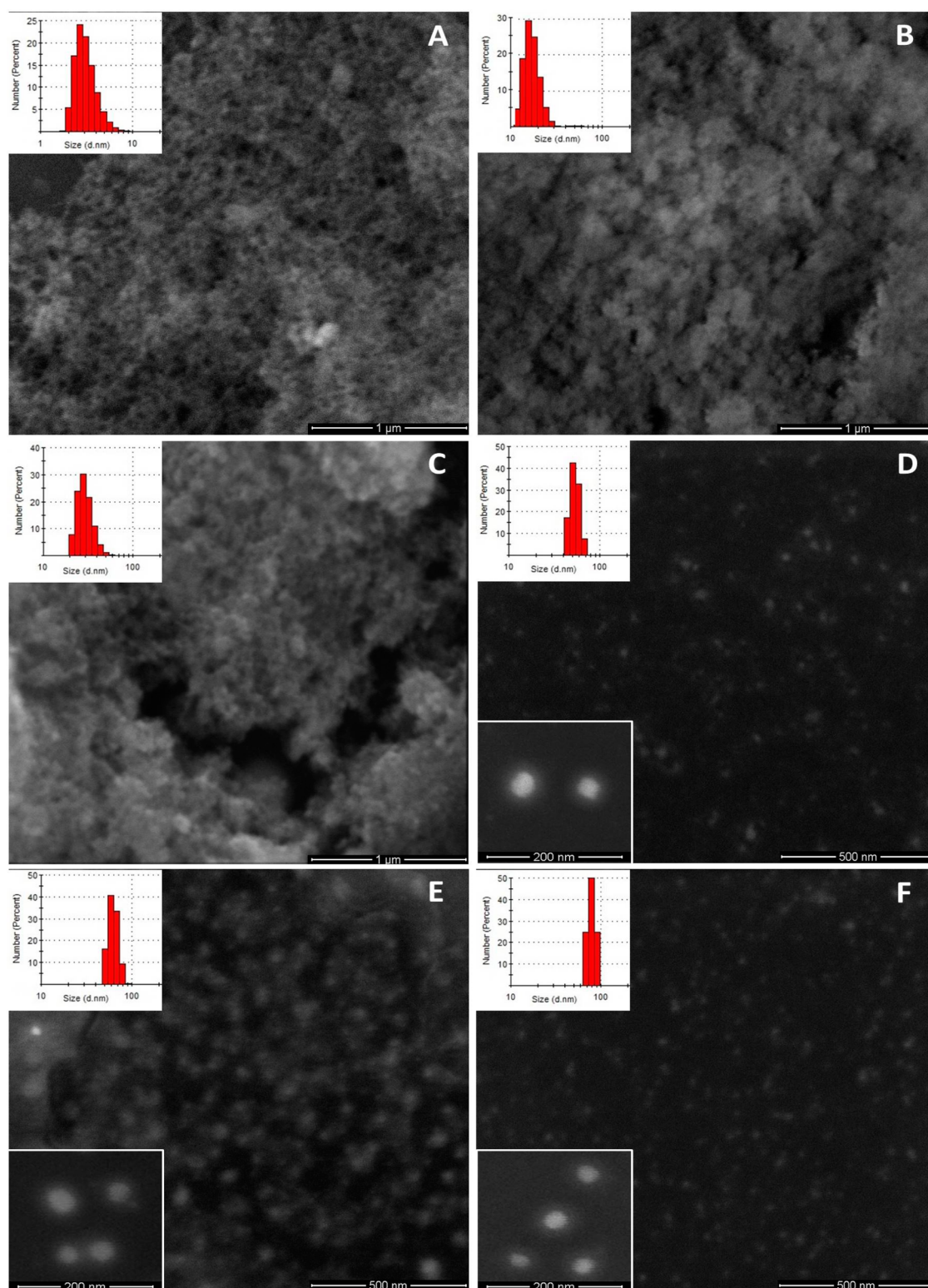


Figure 6. SEM images and size distribution of (a) Fe_3O_4 , (b) $\text{Fe}_3\text{O}_4@SiO_2(\text{FITC})$, (c) $\text{Fe}_3\text{O}_4@SiO_2(\text{FITC})\text{-FA/NH}_2$, and STEM images of (d) $\text{Fe}_3\text{O}_4@SiO_2(\text{FITC})\text{-FA/AICAR}$, (e) $\text{Fe}_3\text{O}_4@SiO_2(\text{FITC})\text{-FA/DOX}$, (f) $\text{Fe}_3\text{O}_4@SiO_2(\text{FITC})\text{-FA/AICAR/DOX}$ nanoparticles.

FTIR spectra of (1) Fe_3O_4 , (2) $\text{Fe}_3\text{O}_4@SiO_2(\text{FITC})$, (3) $\text{Fe}_3\text{O}_4@SiO_2(\text{FITC})\text{-FA}$, (4) $\text{Fe}_3\text{O}_4@SiO_2(\text{FITC})\text{-FA/AICAR}$, (5) $\text{Fe}_3\text{O}_4@SiO_2(\text{FITC})\text{-FA/DOX}$, and (6) $\text{Fe}_3\text{O}_4@SiO_2(\text{FITC})\text{-FA/AICAR/DOX}$ nanoparticles are shown in Figure 4a/b.

The two oxygen atoms of COO in oleic acid provide two coordination positions to form the chemical interaction

with Fe atom. As a result of the chemical interaction, the band 1710 cm^{-1} , which is assigned to the stretching vibration of C=O in free oleic acid, disappeared in the FTIR spectra of Fe_3O_4 and the asymmetric ($-\text{COO}^-$) and symmetric ($-\text{COO}^-$) stretch vibration band resulted at 1430 and 1520 cm^{-1} , respectively. The bands at 2853 and 2924 cm^{-1} are attributed to the asymmetric CH_2 stretch and the symmetric CH_2 stretch

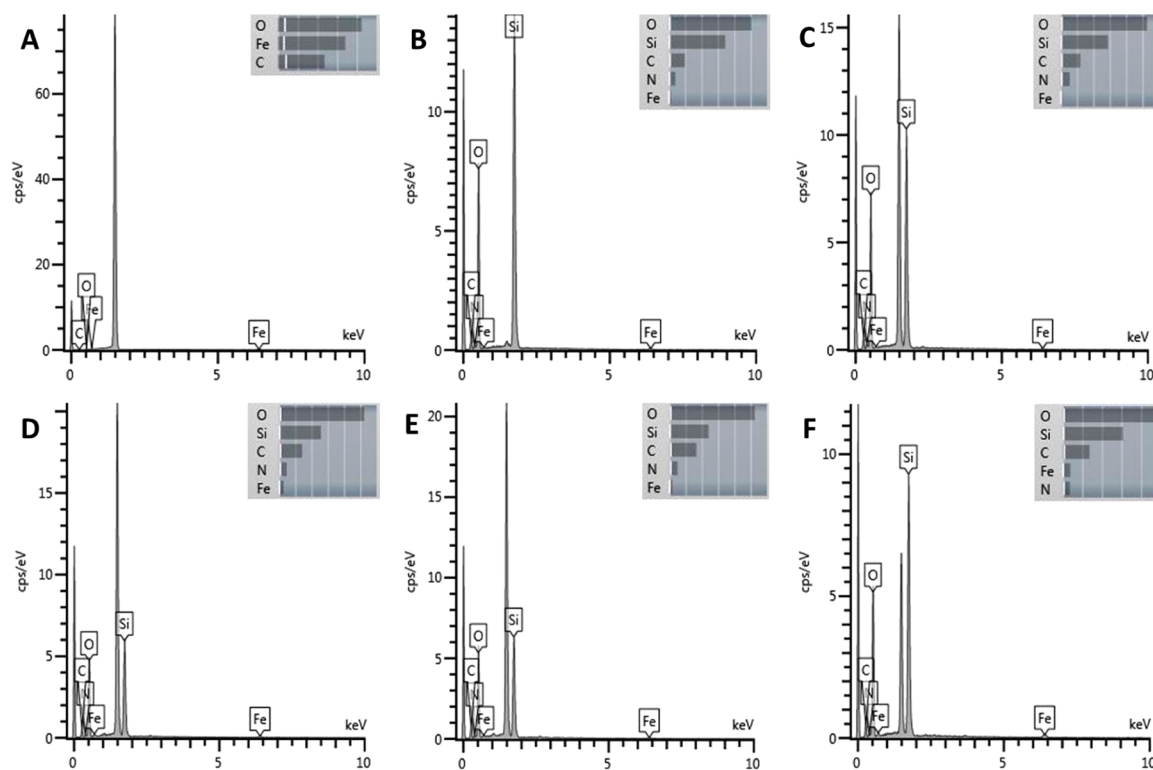


Figure 7. EDX spectra of (a) Fe_3O_4 , (b) $\text{Fe}_3\text{O}_4@SiO_2(\text{FITC})$, (c) $\text{Fe}_3\text{O}_4@SiO_2(\text{FITC})\text{-FA}/\text{NH}_2$, (d) $\text{Fe}_3\text{O}_4@SiO_2(\text{FITC})\text{-FA}/\text{AICAR}$, (e) $\text{Fe}_3\text{O}_4@SiO_2(\text{FITC})\text{-FA}/\text{DOX}$, and (f) $\text{Fe}_3\text{O}_4@SiO_2(\text{FITC})\text{-FA}/\text{AICAR}/\text{DOX}$ nanoparticles (inset: weight percentages of composition), obtained during SEM experiments.

in oleic acid, confirm the presence of the oleic acid on the Fe_3O_4 surface.²⁹ The spectrum of Fe_3O_4 nanoparticles exhibited a strong peak at 584 cm^{-1} which is assigned to typical Fe–O vibrations of the magnetite structure, sustaining the iron oxide identification by XRD.³⁰

In the FTIR spectra of $\text{Fe}_3\text{O}_4@SiO_2(\text{FITC})$, new bands associated with Si–O–Si asymmetric stretching at 1070 cm^{-1} , Si–OH stretching at 950 cm^{-1} , Si–O–Si symmetric stretching at 794 cm^{-1} , and Si–O–Si bending vibrations at 467 cm^{-1} were observed, thus confirming the formation of the silica shells.³¹ The broad band around 3425 cm^{-1} was due to O–H stretching vibrations of adsorbed water and hydrogen-bonded surface silanol groups, whereas the bands around 1548 and 1632 cm^{-1} are attributed to bending of N–H, characteristic of the presence of an NH_2 group.³² Furthermore, a significant decrease in the intensity of the bands related to Fe–O vibrations at 580 cm^{-1} , revealing an increase in the thickness of the silica shells and the complete encapsulation of the magnetic cores, in accordance with the results from XRD and EDX.

The band at 1606 cm^{-1} corresponding to the stretching vibrations of C=C in the backbone of the aromatic ring present in folic acid, indicated the immobilization of folic acid on nanoparticle surfaces. The peak at 1534 cm^{-1} is due to the primary amine group of APTES, indicating that the nanoparticles have been surface modified by amine group. The band at 1585 cm^{-1} , referred to as the stretching vibration of two carbonyl groups of the anthracene ring of DOX,³³ indicated that DOX was successfully attached to the surface of the nanoparticles. The spectral range between 1000 and 800 cm^{-1} is very informative on nucleic acid absorption, due to sugar vibrations sensitive to their conformation and to backbone vibrational modes. Therefore, the bands at 890 and 926 cm^{-1}

indicated that AICAR immobilization with covalent bonding on the surface of the nanoparticles was successfully achieved.³⁴

The grafting density of FA, AICAR, and DOX on nanoparticles was analyzed by measuring the differences of weight loss due to organics decomposition in both $\text{Fe}_3\text{O}_4@SiO_2(\text{FITC})$ and $\text{Fe}_3\text{O}_4@SiO_2(\text{FITC})\text{-FA}/\text{AICAR}/\text{DOX}$ nanoparticles, by TGA (Figure 5). According to the results, the decreased weight of $\text{Fe}_3\text{O}_4@SiO_2(\text{FITC})$ nanoparticles was about 7.77% between 25 and $650\text{ }^\circ\text{C}$, presumably due to the degradation of the organic fluorescent FITC within silica layer. $\text{Fe}_3\text{O}_4@SiO_2(\text{FITC})\text{-FA}/\text{AICAR}/\text{DOX}$ nanoparticles showed a weight loss of 21.20 wt % and exhibited a four-stage weight loss process in the same temperature range, which could be attributed to the presence of substantial amount of FA, AICAR, and DOX molecules. The notable difference (13.43 wt %) between the mass loss of $\text{Fe}_3\text{O}_4@SiO_2(\text{FITC})$ and $\text{Fe}_3\text{O}_4@SiO_2(\text{FITC})\text{-FA}/\text{AICAR}/\text{DOX}$ nanoparticles revealed the successful surface conjugation of the nanoparticles with FA, AICAR, and DOX.

The exterior morphologies and interior structures of the nanoparticles at different fabrication stage were investigated by SEM and STEM, respectively; and the related chemical compositions were determined by EDX.

SEM images showed that the parent iron oxide nanoparticles were nearly spherical and present a narrow size distribution (Figure 6a/b/c). The corresponding EDX spectrum confirmed that the Fe_3O_4 particles are composed of Fe and O, with the C peak indicating the presence of a thin oleic acid shell enveloping the magnetic cores, without any impurity. The untagged Al peak is from the double stick aluminum tape used in sample preparation (Figure 7a and Table 3). After the silica coating, $\text{Fe}_3\text{O}_4@SiO_2(\text{FITC})$ and $\text{Fe}_3\text{O}_4@SiO_2(\text{FITC})\text{-FA}/\text{NH}_2$ nanoparticle morphology remained unchanged. EDX analysis

Table 3. Surface Atomic Percentages of the Nanoparticles, Obtained from EDX Spectra

| nanoparticles | atomic (%) | | | | |
|--|------------|------|------|-----|------|
| | O | Si | C | N | Fe |
| Fe ₃ O ₄ | 51.6 | - | 37.4 | - | 11.0 |
| Fe ₃ O ₄ @SiO ₂ (FITC) | 56.9 | 22.4 | 15.1 | 5.1 | 0.5 |
| Fe ₃ O ₄ @SiO ₂ (FITC)-FA/NH ₂ | 57.5 | 17.9 | 17.4 | 6.9 | 0.3 |
| Fe ₃ O ₄ @SiO ₂ (FITC)-FA/AICAR | 56.1 | 13.1 | 26.3 | 3.8 | 0.7 |
| Fe ₃ O ₄ @SiO ₂ (FITC)-FA/DOX | 53.7 | 14.6 | 25.8 | 5.2 | 0.7 |
| Fe ₃ O ₄ @SiO ₂ (FITC)-FA/AICAR/DOX | 55.5 | 14.7 | 25.5 | 3.5 | 0.8 |

confirmed the existence of Si, a gradual increase in the N content, and a significant decrease in the Fe content, which was still detected due to the penetration depth of the X-ray beam,

thus confirming the encapsulation of the magnetic cores in a thick silica shell (Figure 7b/c). The EDX analysis of Fe₃O₄@SiO₂(FITC)-FA/AICAR, Fe₃O₄@SiO₂(FITC)-FA/DOX, and Fe₃O₄@SiO₂(FITC)-FA/AICAR/DOX nanoparticles clearly showed the progressive increase in C content and reduction in N content on the silica surfaces due to organic functionalities which are gradually enriched by iterative chemical conjugation (Figure 7d/e/f).

The morphologies of the Fe₃O₄@SiO₂(FITC)-FA/AICAR, Fe₃O₄@SiO₂(FITC)-FA/DOX, and Fe₃O₄@SiO₂(FITC)-FA/AICAR/DOX nanoparticles were investigated by STEM. Figure 6d/e/f shows that the nanoparticles have core-shell morphology and spherical shape without aggregation or accumulation.

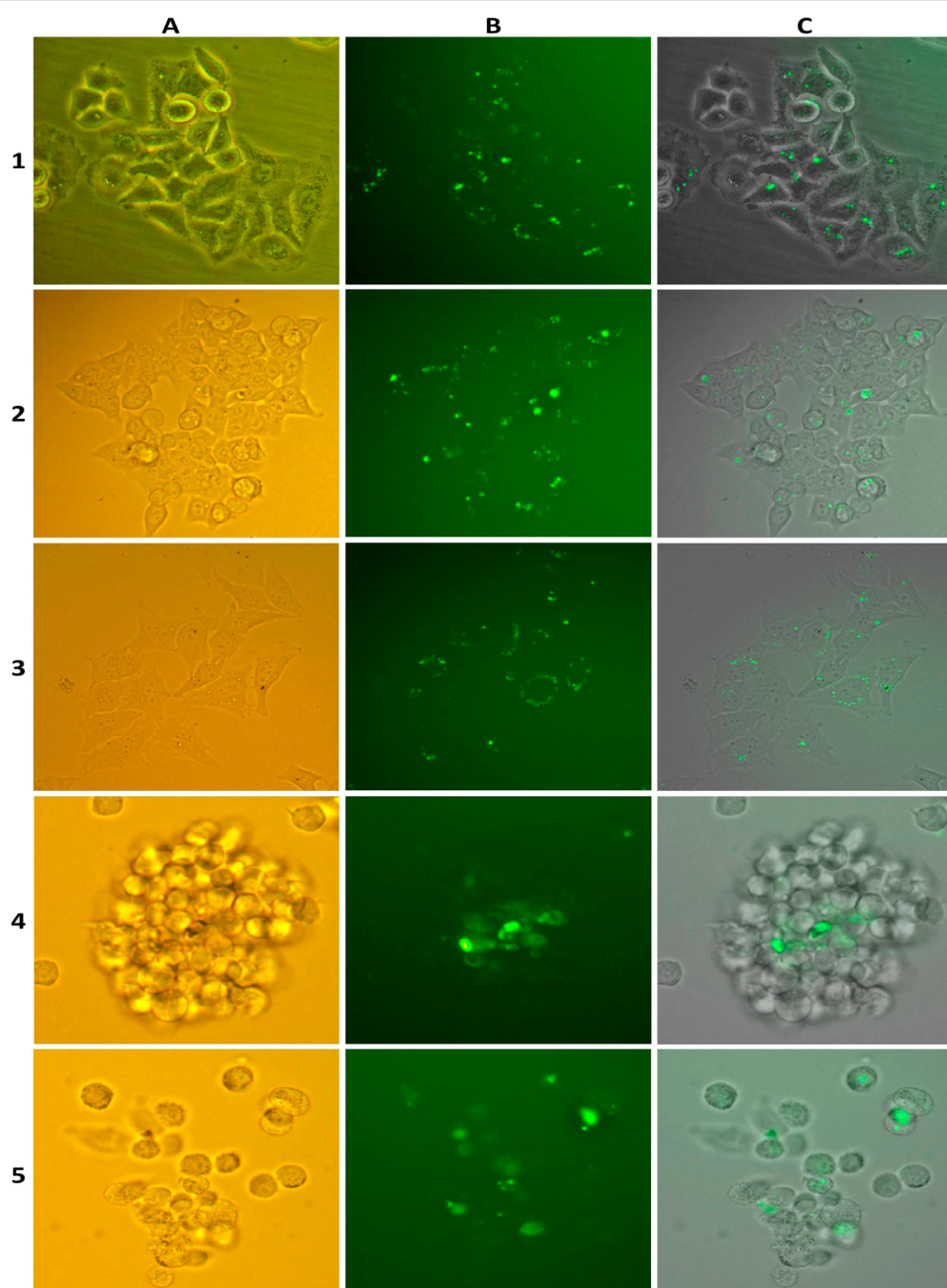


Figure 8. Intracellular localization of the Fe₃O₄@SiO₂(FITC)-FA/AICAR/DOX nanoparticles in cancer cells. For rows: A, bright-field images; B, fluorescence images; C, the merger of both. For columns: 1, A549; 2, HCT-116; 3, HeLa; 4, Jurkat; and 5, MIA PaCa-2 cells.

Table 4. IC₅₀ values of Fe₃O₄@SiO₂(FITC)-FA, Fe₃O₄@SiO₂(FITC)-FA/AICAR, Fe₃O₄@SiO₂(FITC)-FA/DOX, and Fe₃O₄@SiO₂(FITC)-FA/AICAR/DOX Nanoparticles in A549, HCT-116, HeLa, Jurkat, and MIA PaCa-2 Cells When Incubated for 48 h^a

| nanoparticles (μg/mL) | A549 | HCT-116 | HeLa | Jurkat | MIA PaCa-2 |
|--|------------|------------|------------|------------|------------|
| Fe ₃ O ₄ @SiO ₂ (FITC)-FA | N.A. | N.A. | N.A. | N.A. | N.A. |
| Fe ₃ O ₄ @SiO ₂ (FITC)-FA/AICAR | N.A. | N.A. | N.A. | N.A. | N.A. |
| Fe ₃ O ₄ @SiO ₂ (FITC)-FA/DOX | 26.4 ± 1.4 | 48.0 ± 4.8 | 61.2 ± 6.1 | 41.7 ± 2.9 | 48.7 ± 3.8 |
| Fe ₃ O ₄ @SiO ₂ (FITC)-FA/AICAR/DOX | 14.8 ± 4.1 | 49.5 ± 3.0 | 47.5 ± 2.5 | 48.2 ± 3.1 | 58.0 ± 5.2 |

^aN.A. = Not Applicable (the data cannot be fitted as no enough inhibition is observed) in the cancer cells. Values represent the mean ± SD of three independent experiments.

Cellular Uptake. Specificity and cellular accumulation of Fe₃O₄@SiO₂(FITC)-FA/AICAR/DOX nanoparticle vectors by five tumor-derived cell lines (A549, HCT-116, HeLa, Jurkat, and MIA PaCa-2) were confirmed by fluorescence microscopy, which demonstrated intracellular nanoparticle accumulations in each cell line (Figure 8 plots 1–5, rows a–c). The weak green fluorescence in the cytoplasm clearly indicated the successful penetration of the vectors into the cells via folate-receptor-mediated endocytosis. Verification of cellular accumulation of the vectors was obtained by comparing of the fluorescence images with the corresponding bright-field images. The overlay images demonstrated that the magnetic-fluorescent vectors represent a true molecular targeting. These results corroborated the overexpression of folate receptor on A549, HCT-116, HeLa, Jurkat, and MIA PaCa-2 cells, which facilitate the recognition of nanoparticles and increase the uptake through internalization.³⁵

Cytotoxicity of the Multifunctional Nanoparticles. To examine how the conjugation of AICAR with DOX affected its cytotoxicity, we compared the proliferation of A549, HCT-116, HeLa, Jurkat, and MIA PaCa-2 cells treated with the nanoparticle complexes using MTT cell proliferation assay. First, we chose a concentration of DOX (20 μM) 10 times lower than the concentration of AICAR (200 μM) during immobilization processes in terms of minimal growth inhibition in these cells for our combination therapy studies. Next, we investigated whether combination therapy with the inhibitor and drug would be effective at inhibiting tumor cell proliferation and inducing cell death. Cancer cells were exposed to nanoparticles with increasing concentrations of nanoparticles (0.1–200 μg/mL) for 48 h. Among all nanoparticles tested, Fe₃O₄@SiO₂(FITC)-FA/AICAR/DOX nanoparticles showed the lowest IC₅₀ value in A549 cells and led to approximately 1.8-fold decreases in the IC₅₀ values to Fe₃O₄@SiO₂(FITC)-FA/DOX nanoparticles that would be significant in a clinical context (Table 4). The conjugation of AICAR with DOX improved the cytotoxicity not only with a synergistic inhibition, but also with a 30% decreased level of DOX in Fe₃O₄@SiO₂(FITC)-FA/AICAR/DOX nanoparticles. Fe₃O₄@SiO₂(FITC)-FA/AICAR nanoparticles showed low cytotoxicity to all the cells tested, whereas Fe₃O₄@SiO₂(FITC)-FA control nanoparticles did not affect cancer cell viabilities to the same extent (Figure 9). These data showed that Fe₃O₄@SiO₂(FITC)-FA/AICAR/DOX nanoparticles were more effective against A549 and HeLa cells while HCT-116, Jurkat, and MIA PaCa-2 had similar IC₅₀ values. These results indicate that survivin inhibition by AICAR can increase the efficacy of chemotherapy for a wide range of cancer types, which may have important implications for the design of experimental protocols.

We also observed a clear dose-dependent inhibition with Fe₃O₄@SiO₂(FITC)-FA/AICAR/DOX and Fe₃O₄@SiO₂(FITC)-FA/DOX nanoparticles in all the cancer cells

tested. These nanoparticles strongly reduced the proliferation of cancer cells after 48 h of treatment, while a low effect was observed with Fe₃O₄@SiO₂(FITC)-FA/AICAR nanoparticles and no significant effect of the control Fe₃O₄@SiO₂(FITC)-FA nanoparticles. The poor antitumoral efficacy exhibited by Fe₃O₄@SiO₂(FITC)-FA/AICAR indicates that the maximum amount of these nanoparticles in the cells was not sufficient to affect cell viability. This implies that a higher concentration of the nanoparticles would be needed to obtain a notable reduction in cell viability.

As survivin is not a cell surface protein and does not have an intrinsic enzymatic activity, targeting of survivin for therapeutic purposes has been mostly employed at the transcriptional levels.⁶ A number of siRNA-based therapies have been reported as survivin neutralizing agent to increase the sensitivity of cancer cells to DOX and have managed to restore sensitivity to chemotherapeutically induced apoptosis in several cancer cells.^{36,37} However, one of the main hurdles to the application of siRNA-based therapy identified to date is the potential off-target effects. It has been well-documented that delivering siRNA into cells can suppress the expression of genes other than the desired targets.³⁸ To eliminate these obstacles, AICAR could be of potential value for increasing the sensitivity of cancer cells to anticancer drugs, as a small-molecule inhibitor that could be easily incorporated in practice for the down-regulation of survivin.

CONCLUSIONS

Herein we presented successful fabrication and characterization of novel magnetic-fluorescence based, folic acid functionalized nanoparticles for simultaneous delivery of AICAR and DOX into cancer cells. These multifunctional nanoparticles were synthesized by a simple coprecipitation of Fe²⁺/Fe³⁺ salts which were then encapsulated within a SiO₂ shell to provide surface modification and biocompatibility as well as to act as a host for fluorescent dye (FITC). The cancer targeting feature was endowed by conjugating FA on the surface of nanoparticles via an esterification reaction. AICAR and DOX complexes were then successfully attached on the amine-functionalized nanoparticles using Schiff-base chemistry. As far as we know, the synergetic effect of AICAR and DOX has not yet been investigated and this is the first successful preparation of AICAR-DOX conjugated luminomagnetic nanoparticles as a single platform. The structures of the newly synthesized nanoparticles have been confirmed by different characterization techniques: DLS; XRD; FTIR; TGA; EDX; SEM; and STEM. The nanoparticles possess high inhibitor and drug association with good biocompatibility. In addition, the preparation procedure is an environmentally friendly and low-cost synthetic route.

The combination of AICAR and DOX is expected to maximize tumor cell killing by sensitization of cancer cells and

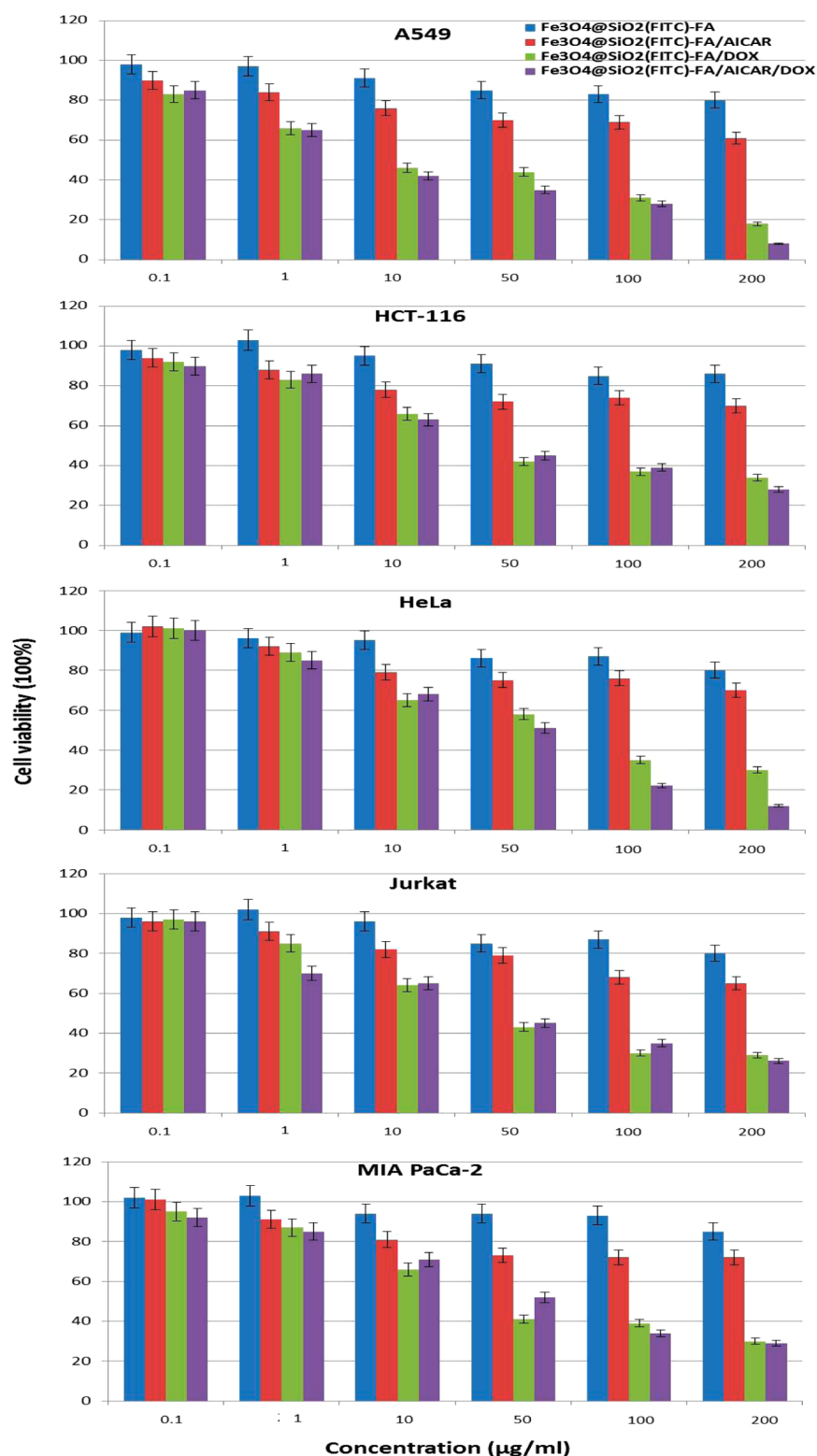


Figure 9. Anticancer activities of Fe₃O₄@SiO₂(FITC)-FA, Fe₃O₄@SiO₂(FITC)-FA/AICAR, Fe₃O₄@SiO₂(FITC)-FA/DOX, and Fe₃O₄@SiO₂(FITC)-FA/AICAR/DOX nanoparticles against A549, HCT-116, HeLa, Jurkat, and MIA PaCa-2 cells after 48 h of growth. The results are expressed as percentage of cell viability or cell number obtained in the untreated controls. The nanoparticle concentrations are expressed as µg nanoparticles per mL. Fe₃O₄@SiO₂(FITC)-FA blank nanoparticles were used as control. Each column represents the mean ± SD of three independent experiments performed in triplicate normalized to nontreated cells (taken as 100%). Note that the amount of DOX conjugation on the surface of Fe₃O₄@SiO₂(FITC)-FA/AICAR/DOX nanoparticles is 30% less than the surface of Fe₃O₄@SiO₂(FITC)-FA/DOX nanoparticles.

to minimize organ toxicity by targeting administration of the inhibitor and drug complex. Fluorescence microscopy and MTT studies confirmed intracellular nanoparticle accumulation

and efficient antitumor activity. We have shown that the cancer cells can be visualized with a low concentration of Fe₃O₄@SiO₂(FITC)-FA/AICAR/DOX nanoparticles (10 µg/mL) with

detectable cell numbers about 10^5 confirming cellular uptake of nanoparticles. Moreover, the nanoparticles not only served as a nanocarrier but also exhibited synergistic cytotoxic activity against the cancer cells. We have demonstrated that combination therapy with $\text{Fe}_3\text{O}_4@\text{SiO}_2(\text{FITC})\text{-FA/AICAR/DOX}$ nanoparticles is superior to monotherapy with nanoparticles decorated with either AICAR or DOX alone. Importantly, the combination effects of the nanoparticles were confirmed in five different cancer cell lines. Our data indicate a strong effect of $\text{Fe}_3\text{O}_4@\text{SiO}_2(\text{FITC})\text{-FA/AICAR/DOX}$ nanoparticles on the lung carcinoma A549 and the cervical carcinoma HeLa cell lines, while similar outcomes were observed on the colon carcinoma HCT-116, the leukemia Jurkat, and the pancreatic carcinoma MIA PaCa-2 cell lines. We believe that this combination will be a valuable addition in the sensitization of cancer cells toward anticancer drugs to improve the therapeutic outcome of chemotherapy. Finally, it could be concluded that coadministration of AICAR and DOX might promote apoptosis more than each drug alone or incubation of one compound prior to the other one. The characterization of apoptotic and antiproliferative effects and related caspase-3 activity studies of the nanoparticles are currently under investigation.

MATERIAL AND METHODS

Materials. Iron(II) chloride tetrahydrate ($\text{FeCl}_2\cdot 4\text{H}_2\text{O}$) (99%), iron(III) chloride hexahydrate ($\text{FeCl}_3\cdot 6\text{H}_2\text{O}$) (98%), 3-aminopropyltriethoxysilane (APTES), tetraethyl orthosilicate 99.9% (TEOS), *N*-hydroxysuccinimide (NHS), *N,N*-dicyclohexylcarbodiimide (DCC), fluorescein isothiocyanate (FITC), folic acid (FA), dimethyl sulfoxide (DMSO), triton X-100, FT-IR grade potassium bromide $\geq 99\%$ (KBr), Glutaraldehyde 25% aqueous solution, 5-aminoimidazole-4-carboxamide-1- β -D-ribofuranoside $\geq 98\%$ (AICAR), and 3-[4,5-dimethyl-2-thiazolyl]-2,5-diphenyltetrazolium bromide (MTT) were purchased from Sigma-Aldrich Chemicals. Oleic acid (99%), cyclohexane, 1-hexanol ($>98\%$), ammonium hydroxide 25% aqueous solution, and toluene were purchased from Fluka/Riedel-de Haën Chemicals. Doxorubicin was obtained from SABA Pharma. DMEM growth medium, RPMI-1640 growth medium, 10% fetal bovine serum (FBS), streptomycin, penicillin, and L-glutamic acid were purchased from Gibco Life Technologies. All other chemicals and reagents were of the highest purity. All the experiments were performed in deionized Milli-Q water.

Cell Cultures. A549 (human epithelial lung carcinoma), HCT-116 (human epithelial colorectal carcinoma), HeLa (human epithelial cervical carcinoma), Jurkat (human acute T-cell leukemia), and MIA PaCa-2 (human epithelial pancreatic carcinoma) cell lines were kindly provided by Biotechnology and Bioengineering Research and Application Centre, Izmir Institute of Technology, Turkey. A549, HCT-116, HeLa, and MIA PaCa-2 cancer cells were cultured in Dulbecco's modified Eagle medium (DMEM) supplemented with 10% fetal bovine serum (FBS), 100 $\mu\text{g}/\text{mL}$ streptomycin, 100 U/mL penicillin, and 2 mM L-glutamic acid; Jurkat cancer cells were cultured in Roswell Park Memorial Institute-1640 (RPMI-1640) growth medium supplemented with 10% fetal bovine serum (FBS), 100 $\mu\text{g}/\text{mL}$ streptomycin, 100 U/mL penicillin, and 2 mM L-glutamic acid. All cell lines were incubated in 5% CO_2 and 90–100% relative humidity at 37 °C. Medium renewal was carried out 2 to 3 times per week, and cells were subcultured when they achieved 80–90% confluence. All cell lines were

discarded after 20 generations, and new lines were obtained from frozen stocks.

Synthesis of Multifunctional Nanoparticles. *Synthesis of Oleic Acid Coated Fe_3O_4 Nanoparticles.* Oleic acid coated iron oxide (Fe_3O_4) nanoparticles were synthesized by coprecipitation of Fe^{2+} and Fe^{3+} salts with a stoichiometric ratio of 1:2 in accordance with the chemical reaction formula: $[\text{Fe}^{2+} + 2\text{Fe}^{3+} + 8\text{OH}^- = \text{Fe}_3\text{O}_4 + 4\text{H}_2\text{O}]$. Since oleic acid effectively regulates Fe_3O_4 nanoparticles growth and prevents aggregation,²⁰ in this step we determined the oleic acid concentration to obtain surfactant-stabilized and narrow size distributed Fe_3O_4 nanoparticles. First, 0.456 g $\text{FeCl}_3\cdot 6\text{H}_2\text{O}$ and 0.189 g $\text{FeCl}_2\cdot 4\text{H}_2\text{O}$ were dissolved in 100 mL ultrapure water under nitrogen environment with ultrasonification for 10 min. NH_4OH (25%) aqueous solution was added dropwise until pH 10–11. After base had been added, the alkaline solution started to become dark brown. Oleic acid (0.1/0.2/0.4/0.6 mL) was added immediately to the dark brown solution and the resulting emulsion was aged, under vigorous mechanical stirring, at room temperature for 1 h. Then the emulsion was heated up to 95 °C to convert iron hydroxides into magnetite. As soon as that temperature was reached, the suspension was cooled down to room temperature. The mixture was then acidified to pH 5–6 by using a HNO_3 solution (35%) to promote the chemisorption of oleate ions on the magnetite particles. Consequently, the particles coagulated and precipitated in the solution due to the hydrophobicity provided by the oleate layer. The resulting magnetic particles settled within a few minutes and were then washed with ultrapure water four times to remove the unreacted salts and with ethanol three times to remove water and nonadsorbed oleic acid. Finally, the oleic acid coated nanoparticles were dried in vacuum oven at room temperature for 12 h.

Synthesis of $\text{Fe}_3\text{O}_4@\text{SiO}_2(\text{FITC})$ Nanoparticles. Silica core-shell nanoparticles [$\text{Fe}_3\text{O}_4@\text{SiO}_2(\text{FITC})$] were synthesized by a water-in-oil reverse micelle method with some modification of a published procedure in two steps.²¹ In the first step, the oleic acid protected Fe_3O_4 nanoparticles were coated with a thin silica shell by hydrolysis and condensation of TEOS as sol-gel precursor. Briefly, a microemulsion system was prepared with 10 mg of dried magnetic Fe_3O_4 powder added to 0.3 mL TEOS, 70 mL cyclohexane, 20 g Triton X-100 (as surfactant), 15 mL *n*-hexanol (as cosurfactant), and 3.7 mL H_2O mixture with intense stirring at room temperature. Six hours later, 1.0 mL aqueous NH_4OH (25%) was introduced dropwise to initiate TEOS hydrolysis and the microemulsion was kept stirring for another 24 h. In the second step, after the first silica shell had been coated on the magnetic core, the dye molecules were encapsulated into the second silica shell to enhance photochemical stability. FITC-APTES conjugate was prepared by covalently attaching FITC to the APTES silane compound by a stable thiourea linkage. Briefly, 1.0 mg FITC and 0.15 mL APTES were combined together in 0.2 mL of absolute ethanol under nitrogen atmosphere and stirred in orbital shaker for 24 h. The FITC-APTES conjugate solution was protected from light during reaction and storage to prevent photobleaching. After 24 h, FITC-APTES ethanolic solution and 0.3 mL TEOS were added to the first microemulsion under stirring in dark for 24 h. Finally, ethanol was added to destabilize the microemulsion system. The FITC-incorporated silica-coated core-shell [$\text{Fe}_3\text{O}_4@\text{SiO}_2(\text{FITC})$] nanoparticles were collected via centrifugation and washed in sequence with ethanol and

ultrapure water to remove any surfactant and unreacted reactants and dried by air.

Synthesis of $\text{Fe}_3\text{O}_4@/\text{SiO}_2(\text{FITC})\text{-FA}/\text{NH}_2$ Nanoparticles. The $\text{Fe}_3\text{O}_4@/\text{SiO}_2(\text{FITC})\text{-FA}/\text{NH}_2$ nanoparticles were prepared according to a literature procedure with some modification.²² First, folic acid was conjugated with APTES by an esterification reaction of the carboxyl group with the amine group. In brief, an APTES ester of FA (FA-APTES) was prepared by mixing folate (4.0 mg) with APTES (2.0 μL) in 40 mL dry dimethyl sulfoxide (DMSO) in the presence of NHS (1.1 mg) and DCC (4.7 mg) as the catalyst at room temperature for 2 h. After this, a mixture of $\text{Fe}_3\text{O}_4@/\text{SiO}_2(\text{FITC})$ nanoparticles (100 mg), FA-APTES conjugate, and free APTES (17 μL) in toluene (160 mL) was stirred at room temperature for 24 h to introduce FA-APTES conjugate and free APTES (to provide a linker for the subsequent conjugation of both AICAR and DOX) on the surface of silica-coated nanoparticles by hydrolysis and condensation of APTES through silanization. Final products were collected by a magnet, washed with toluene and ethanol several times to remove any unreacted reactants, and dried in a vacuum oven at room temperature, overnight.

Synthesis of $\text{Fe}_3\text{O}_4@/\text{SiO}_2(\text{FITC})\text{-FA}/\text{AICAR}/\text{DOX}$ Nanoparticles. $\text{Fe}_3\text{O}_4@/\text{SiO}_2(\text{FITC})\text{-FA}/\text{AICAR}/\text{DOX}$ were prepared by coupling of AICAR and DOX complexes on the surface of amine-modified nanoparticles via glutaraldehyde activation. In this step three successive nanoparticles were synthesized to evaluate the synergistic potential of therapeutics: (1) $\text{Fe}_3\text{O}_4@/\text{SiO}_2(\text{FITC})\text{-FA}/\text{AICAR}$ nanoparticles containing only inhibitor; (2) $\text{Fe}_3\text{O}_4@/\text{SiO}_2(\text{FITC})\text{-FA}/\text{DOX}$ nanoparticles containing only drug; (3) $\text{Fe}_3\text{O}_4@/\text{SiO}_2(\text{FITC})\text{-FA}/\text{AICAR}/\text{DOX}$ nanoparticles containing both inhibitor and drug. Furthermore, since glutaraldehyde is a very reactive reagent,²³ different concentrations of glutaraldehyde were tested separately to determine the optimal linker concentration. First of all, the surface of $\text{Fe}_3\text{O}_4@/\text{SiO}_2(\text{FITC})\text{-FA}/\text{NH}_2$ nanoparticles (10 mg) was activated with glutaraldehyde (0.1–1.0%) in 20 mL ultrapure water under vigorous mechanical stirring at room temperature for 30 min. Then, nanoparticles were collected via centrifugation and the unreacted glutaraldehyde was removed by comprehensive washing with ultrapure water. Glutaraldehyde activated nanoparticles were subsequently incubated with AICAR (200 μM) and DOX (20 μM) complexes in 20 mL ultrapure water under vigorous mechanical stirring at room temperature for 6 h. For AICAR and DOX conjugation, an excess amount of AICAR (molar ratio of AICAR to DOX = 10) was used to evaluate the sensitization effect of AICAR with low-dose DOX concentration. The resulting nanoparticles [(1) $\text{Fe}_3\text{O}_4@/\text{SiO}_2(\text{FITC})\text{-FA}/\text{AICAR}$; (2) $\text{Fe}_3\text{O}_4@/\text{SiO}_2(\text{FITC})\text{-FA}/\text{DOX}$; (3) $\text{Fe}_3\text{O}_4@/\text{SiO}_2(\text{FITC})\text{-FA}/\text{AICAR}/\text{DOX}$] were magnetically separated and washed with ultrapure water several times to remove any unreacted reactants and dried under vacuum at room temperature, overnight.

Structural and Physicochemical Characterization. Dynamic light scattering (DLS) measurements were performed at 25 °C, using a Malvern Zetasizer NanoZS compact scattering spectrometer. The average hydrodynamic diameters, the size distributions and the surface charge analysis of the samples were determined using Malvern Dispersion Technology Software 7.11. Nanoparticles were suspended in ultrapure water (Fe_3O_4 nanoparticles in hexane) to give optimum signal intensity. All measurements were repeated three times to verify the reproducibility of the results.

Powder X-ray diffraction (XRD) measurements were performed with “Philips X’Pert Pro”, at room temperature by using Cu $K\alpha$ radiation ($\lambda = 1.5405 \text{ \AA}$) and Bragg–Brentano $\theta/2\theta$ configuration. The measurements were performed over the 2θ range of 15–70°.

The Fourier transform infrared spectroscopy (FTIR) spectra of the nanoparticles were collected with a “PerkinElmer Spectrum-100” spectrophotometer in the range 450–4000 cm^{-1} . The spectra of the dried samples were obtained by employing a KBr pellet.

Thermogravimetric analysis (TGA) was performed on a PerkinElmer Diomand TG/DTA Instruments from room temperature to 650 °C with a heating rate of 10 °C/min in a nitrogen flow.

Scanning electron microscopy (SEM) and energy-dispersive X-ray spectroscopy (EDX) studies were performed at a high resolution environmental scanning electron microscope (FEI Quanta 250 FEG) equipped with an energy-dispersive X-ray spectrometer (Oxford AZtec). Prior to examination, the lyophilized nanoparticles were placed on a double stick tape over aluminum stubs to get a uniform layer of particles.

Scanning transmission electron microscopy (STEM) images of the final nanoparticles were obtained with a “FEI Quanta 250 FEG” microscope operating with STEM Detector. The nanoparticles were dispersed in water under sonication and a drop was placed on a carbon-coated 400 mesh copper grid followed by air-drying.

Cellular Uptake Analysis. Internalization of the nanoparticles was visualized using an Olympus IX2-ILL100 fluorescence microscope equipped with an appropriate filter set. Images were acquired using a CCD camera and analyzed using ImageJ advanced version software. A549, HCT-116, HeLa, Jurkat, and MIA PaCa-2 cells (1×10^5 cells/well) were seeded in 12-well plates overnight before experiments. $\text{Fe}_3\text{O}_4@/\text{SiO}_2(\text{FITC})\text{-FA}/\text{AICAR}/\text{DOX}$ nanoparticles were added into the incubation medium at concentrations of 10 $\mu\text{g}/\text{mL}$ for 4 h incubation in 5% CO_2 at 37 °C. All cells except Jurkat (suspension cells) and MIA PaCa-2 (suspension/adherent mixed cells) were washed twice with phosphate-buffered saline (PBS). Microscopic images in the green channel for detection of the FITC label encapsulated in nanoparticles and in the bright-field were obtained by fluorescence microscopy.

Cytotoxicity of Multifunctional Nanoparticles. The cytotoxicity of the prepared nanoparticles were evaluated by 3-(4,5-dimethylthiazol-2-yl)-2,5-diphenyltetrazolium bromide (MTT) assay. A549, HCT-116, HeLa, Jurkat, and MIA PaCa-2 cells were seeded into 96-well plates at a density of 1×10^4 per well in 100 μL of media and grown overnight. The cells were then incubated with various concentrations (0.1/1.0/10/50/100/200 $\mu\text{g}/\text{mL}$) of nanoparticles for 48 h at 37 °C under 5% CO_2 . Following this incubation, cells were incubated in medium containing 0.5 mg/mL of MTT for 4 h. The medium was discarded, and the precipitated formazan violet crystals were dissolved in 150 μL of DMSO to solubilize the formazan. After shaking the plate for 10 min, the absorbance of the sample was measured at 570 nm by multidetection microplate reader. The absorbance of dissolved formazan in the visible region correlates with the number of intact active cells. The cytotoxicity was evaluated with reference to the IC_{50} value that was defined as the concentration needed for a 50% reduction of survival based on the survival curves. IC_{50} values were calculated from dose–response curves (nanoparticle concentration vs cell survival fraction) obtained in multireplicated

experiments. For the combination treatment studies, the cells were incubated with (1) $\text{Fe}_3\text{O}_4@\text{SiO}_2(\text{FITC})\text{-FA}$ blank nanoparticles as control, (2) $\text{Fe}_3\text{O}_4@\text{SiO}_2(\text{FITC})\text{-FA/AICAR}$ nanoparticles containing only inhibitor, (3) $\text{Fe}_3\text{O}_4@\text{SiO}_2(\text{FITC})\text{-FA/DOX}$ nanoparticles containing only drug, or (4) $\text{Fe}_3\text{O}_4@\text{SiO}_2(\text{FITC})\text{-FA/AICAR/DOX}$ nanoparticles containing both inhibitor and drug to test the efficacy of nanoparticles on cancer cell growth.

Statistical Analysis. All data were represented as means \pm standard deviation (SD). Statistical analysis was performed with the Student's *t* test, using Excel Software (Microsoft). A *P* value of ≤ 0.05 was considered statistically significant.

AUTHOR INFORMATION

Corresponding Author

*E-mail: cenkdaglioglu@iyte.edu.tr. Phone: +90 232 750 7319. Fax: +90 232 750 7303.

Notes

The authors declare no competing financial interest.

ACKNOWLEDGMENTS

The authors would like to thank Professor Anne Fray for proofreading of the manuscript and staff of The Center for Materials Research of Izmir Institute of Technology for their technical support.

REFERENCES

- (1) Longley, D. B., and Johnston, P. G. (2005) Molecular mechanisms of drug resistance. *J. Pathol.* 205, 275–292.
- (2) Chabner, B. A., and Roberts, T. G., Jr. (2005) Timeline: Chemotherapy and the war on cancer. *Nat. Rev. Cancer* 5, 65–72.
- (3) Yague, E., and Raguz, S. (2005) Drug resistance in cancer. *Br. J. Cancer* 93, 973–976.
- (4) Pennati, M., Folini, M., and Zaffaroni, N. (2007) Targeting survivin in cancer therapy: fulfilled promises and open questions. *Carcinogenesis* 28, 1133–9.
- (5) Fukuda, S., and Pelus, L. M. (2006) Survivin, a cancer target with an emerging role in normal adult tissues. *Mol. Cancer Ther.* 5, 1087–98.
- (6) Pennati, M., Folini, M., and Zaffaroni, N. (2008) Targeting survivin in cancer therapy. *Expert Opin. Ther. Targets* 12 (4), 463–476.
- (7) Meli, M., Pennati, M., Curto, M., Daidone, M. G., Plescia, J., Toba, S., Altieri, D. C., Zaffaroni, N., and Colombo, G. (2006) Small-molecule targeting of heat shock protein 90 chaperone function: rational identification of a new anticancer lead. *J. Med. Chem.* 49, 7721–7730.
- (8) Kizek, R., Adam, V., Hrabeta, J., Eckschlagler, T., and Smutny, S. (2012) Anthracyclines and ellipticines as DNA-damaging anticancer drugs: recent advances. *Pharmacol. Ther.* 133, 26–39.
- (9) Smith, L., Watson, M. B., and O’Kane, S. L. (2006) The analysis of doxorubicin resistance in human breast cancer cells using antibody microarrays. *Mol. Cancer Ther.* 5, 2115–2120.
- (10) Minotti, G., Menna, P., Salvatorelli, E., Cairo, G., and Gianni, L. (2004) Anthracyclines: molecular advances and pharmacologic developments in antitumor activity and cardiotoxicity. *Pharmacol. Rev.* 56, 185–229.
- (11) Gao, J. H., Gu, H. W., and Xu, B. (2009) Multifunctional magnetic nanoparticles: design, synthesis, and biomedical applications. *Acc. Chem. Res.* 42, 1097–1107.
- (12) Wang, X., Ramstrom, O., and Yan, M. (2011) Dye-doped silica nanoparticles as efficient labels for glycans. *Chem. Commun.* 47, 4261–4263.
- (13) Kim, J., Piao, Y., Lee, N., Park, Y. I., Lee, I.-H., Lee, J.-H., Paik, S. R., and Hyeon, T. (2010) Magnetic nanocomposite spheres decorated with NiO nanoparticles for a magnetically recyclable protein separation system. *Adv. Mater.* 22, 57–60.
- (14) Lee, J. E., Lee, N., Kim, H., Kim, J., Choi, S. H., Kim, J. H., Kim, T., Song, I. C., Park, S. P., Moon, W. K., et al. (2010) Uniform mesoporous dye-doped silica nanoparticles decorated with multiple magnetite nanocrystals for simultaneous enhanced magnetic resonance imaging, fluorescence imaging, and drug delivery. *J. Am. Chem. Soc.* 132, 552–7.
- (15) Pan, Y., Du, X., Zhao, F., and Xu, B. (2012) Magnetic nanoparticles for the manipulation of proteins and cells. *Chem. Soc. Rev.* 41, 2912–2942.
- (16) Mulder, W. J. M., Koole, R., Brandwijk, R. J., Storm, G., Chin, P. T. K., Strijkers, G. J., de Mello Donega, C., Nicolay, K., and Griffioen, A. W. (2006) Quantum dots with a paramagnetic coating as a bimodal molecular imaging probe. *Nano Lett.* 6, 1–6.
- (17) Zhao, X., Li, H., and Lee, R. J. (2008) Targeted drug delivery via folate receptors. *Expert Opin. Drug Delivery* 5, 309–319.
- (18) Lu, Y., and Low, P. S. (2002) Folate-mediated delivery of macromolecular anticancer therapeutic agents. *Adv. Drug Delivery Rev.* 54, 675–693.
- (19) Reddy, J. A., Allagadda, V. M., and Leamon, C. P. (2005) Targeting therapeutic and imaging agents to folate receptor positive tumors. *Curr. Pharm. Biotechnol.* 6, 131–150.
- (20) Hyeon, T., Lee, S. S., Park, J., Chung, Y., and Na, H. B. (2001) Synthesis of highly crystalline and monodisperse maghemite nanocrystallites without a size-selection process. *J. Am. Chem. Soc.* 123, 12798–12801.
- (21) Lu, C.-W., Hung, Y., Hsiao, J.-K., Yao, M., Chung, T.-H., Lin, Y.-S., Wu, S.-H., Hsu, S.-Ch., Liu, H.-M., Mou, C.-Y., et al. (2007) Bifunctional magnetic silica nanoparticles for highly efficient human stem cell labeling. *Nano Lett.* 7 (1), 149–154.
- (22) Pereira, C., Pereira, A. M., Quaresma, P., Tavares, P. B., Pereira, E., Araújo, J. P., and Freire, C. (2010) Superparamagnetic- $\text{Fe}_2\text{O}_3@\text{SiO}_2$ nanoparticles: a novel support for the immobilization of [VO(acac)₂]. *Dalton Trans.* 39 (11), 2842–2854.
- (23) Daglioglu, C., and Zihnioglu, F. (2012) Covalent immobilization of trypsin on glutaraldehyde-activated silica for protein fragmentation. *Artif. Cells Blood Subst. and Biotechnol.* 40, 378–384.
- (24) Yoon, T. J., Kim, J. S., Kim, B. G., Yu, K. N., Cho, M. H., and Lee, J. K. (2005) Multifunctional nanoparticles possessing a “Magnetic Motor Effect” for drug or gene delivery. *Angew. Chem., Int. Ed.* 44, 1068–1071.
- (25) Lopez, K. A., Pina, M. N., Alemany, R., Vogler, O., Barcelo, F., and Morey, J. (2014) Antifolate-modified iron oxide nanoparticles for targeted cancer therapy: inclusion vs. covalent union. *RSC Adv.* 4, 19196–19204.
- (26) Laurent, S., Forge, D., Port, M., Roch, A., Robic, C., vander Elst, L., and Muller, R. N. (2008) Magnetic iron oxide nanoparticles: synthesis, stabilization, vectorization, physicochemical characterizations, and biological applications. *Chem. Rev.* 108 (6), 2064–2110.
- (27) Zhang, M., Cushing, B. L., and O’Connor, C. J. (2008) Synthesis and characterization of monodisperse ultra-thin silica-coated magnetic nanoparticles. *Nanotechnology* 19, 085601.
- (28) Li, Y., Dong, C., Chu, J., Qi, J., and Li, X. (2011) Surface molecular imprinting onto fluorescein-coated magnetic nanoparticles via reversible addition fragmentation chain transfer polymerization: A facile three-in-one system for recognition and separation of endocrine disrupting chemicals. *Nanoscale* 3, 280.
- (29) Yang, K., Peng, H., Wen, Y., and Li, N. (2010) Re-examination of characteristic FTIR spectrum of secondary layer in bilayer oleic acid-coated Fe_3O_4 nanoparticles. *Appl. Surf. Sci.* 256, 3093–3097.
- (30) Belin, T., Guigue-Millot, N., Caillot, T., Aymes, D., and Niepe, J. C. (2002) Influence of grain size, oxygen stoichiometry, and synthesis conditions on the $\gamma\text{-Fe}_2\text{O}_3$ vacancies ordering and lattice parameters. *J. Solid State Chem.* 163, 459–465.
- (31) Palma, R., de Trekker, J., Peeters, S., Van Bael, M. J., Bonroy, K., Wirix-Speetjens, R., Reekmans, G., Laureyn, W., Borghs, G., and Maes, G. (2007) Surface modification of $\text{g-Fe}_2\text{O}_3@\text{SiO}_2$ magnetic nanoparticles for the controlled interaction with biomolecules. *J. Nanosci. Nanotechnol.* 7 (12), 4626–41.

(32) Dutta, R. K., Sharma, P. K., and Pandey, A. C. (2010) Design and surface modification of potential luminomagnetic nanocarriers for biomedical applications. *J. Nanopart. Res.* 12, 1211–1219.

(33) Muhammad, F., Guo, M., Guo, Y., Qi, W., Qu, F., Sun, F., Zhao, H., and Zhu, G. (2011) Acid degradable ZnO quantum dots as a platform for targeted delivery of an anticancer drug. *J. Mater. Chem.* 21, 13406–13412.

(34) Ami, D., Mereghetti, P., and Doglia, S. M. (2013) Multivariate analysis for fourier transform infrared spectra of complex biological systems and processes. *Multivariate Analysis in Management, Engineering and the Sciences* (Freitas, L., MSc., Ed.) ISBN: 978-953-51-0921-1. DOI: [10.5772/53850](https://doi.org/10.5772/53850)

(35) Sudimack, J., and Lee, R. J. (2000) Targeted drug delivery via the folate receptor. *Adv. Drug Delivery Rev.* 41, 147–162.

(36) Yonesaka, K., Tamura, K., Kurata, T., Satoh, T., Ikeda, M., Fukuoka, M., and Nakagawa, K. (2006) Small interfering RNA targeting survivin sensitizes lung cancer cell with mutant p53 to Adriamycin. *Int. J. Cancer* 118, 812–820.

(37) Ghosh, S. K., Yigit, M. V., Uchida, M., Ross, A. W., Barteneva, N., Moore, A., and Medarova, Z. (2014) Sequence-dependent combination therapy with doxorubicin and a survivin-specific small interfering RNA nanodrug demonstrates efficacy in models of adenocarcinoma. *Int. J. Cancer* 134 (7), 1758–1766.

(38) Jackson, A. L., and Linsley, P. S. (2010) Recognizing and avoiding siRNA off-target effects for target identification and therapeutic application. *Nat. Rev. Drug Discovery* 9 (1), 57–67.